ChemElectroChem

Research Article
doi.org/10.1002/celc.202400391

Chemistry Europe
European Chemical Societies Publishing

www.chemelectrochem.org

Is Cobalt in Li-Rich Layered Oxides for Li-Ion Batteries Necessary?

Hyeongseon Choi,[a, b] Annika Regitta Schuer,[a, b] Hyein Moon,[a, b] Georgian Melinte,[b, c] Guk-Tae Kim,[a, b] Jakob Asenbauer,[a, b] Arefeh Kazzazi,[a, b] Matthias Kuenzel,*[a, b] and Stefano Passerini*[a, b]

Cobalt is considered an essential element for layered cathode active materials supporting enhanced lithium-ion conductivity and structural stability. Herein, we investigated the influence of Co concentration on the physicochemical properties and electrochemical performance of lithium-rich layered oxides (LRLOs) with different Co content ($Li_{1.2}Ni_{0.2-x/2}Mn_{0.6-x/2}Co_xO_2$, $x = 0$, 0.04, and 0.08). Though the presence of Co grants structural stability to LRLOs, superior long-term cycling stability is achieved with the Co-free LRLO retaining 88.1% of the initial specific capacity (vs. 75.9% of $Li_{1.2}Ni_{0.16}Mn_{0.56}Co_{0.08}O_2$) after 300 galvanostatic cycles at 250 mA g^{-1} (1 C). The chemical stability on the surface of LRLOs containing Co declines faster, indicating a higher bulk structural stability not being the primary determinant of the LRLOs' cycling performance. Ex-situ investigations indicate that the superior cycling stability of Co-free LRLO is obtained by reducing the Mn-related redox at discharge, which contributes to the large degree of polarization and low energy efficiency. Finally, the full-cell configured with the optimized LRLO as cathode and graphite anode delivers an energy density of 464 Wh kg^{-1} at C/10, and 74.4% and 94.3% of retention in discharge specific capacity and average voltage at the 1000th cycle, demonstrating the applicability of Co-free LRLO for sustainable LIBs.

Introduction

LIBs are the most important electric energy storage technology of our time, powering not only mobile electric applications such as laptops and cellphones, but also playing a vital role in shaping future transportation that relies heavily on electric vehicles (EVs). The rapid expansion of the EV market in the last decade raises the importance of tailoring LIB performance for high-energy density applications, creating smaller, thinner, and lighter batteries.[1–4] Lithium is the ideal candidate to meet the demands for evolving volume and weight sensitive applications owing to its lowest electrochemical potential, enabling high cell voltages, and energy-to-weight ratio. As a result, LIBs can achieve large specific and volumetric energy taking advantage of the high working voltages.[5,6] Nonetheless, it is crucial to develop high-performance cathode materials as this is still the main factor determining the general performance of the LIB cell.[7,8] Today's prominent cathode materials are $LiCoO_2$ (LCO), $LiNi_xCo_yMn_zO_2$ (NCM, $x+y+z=1$), $LiMn_2O_4$ (LMO), $LiNi_{0.5}Mn_{1.5}O_4$ (LNMO), and $LiFePO_4$ (LFP), all containing environmentally/economically critical elements (*i.e.*, Co and Ni)[9] with the exception of the latter.[10] Specifically, Co has several issues not just because of its low reserves, but it is also highly toxic and is mined under hazardous conditions. Thus, research efforts are needed to minimize (or eliminate) Co in (from) LIBs' cathode materials.[9,11,12]

In terms of specific energy density and environmental benignity, Co-free Li-rich layered oxide ($Li_{1+x}(Ni_aMn_b)_{1-x}O_2$, $a+b=1$ or $\alpha Li_2MnO_3\cdot(1-\alpha)LiMO_2$ (M=Mn and Ni)) has become the most promising candidate for next-generation LIBs.[13–18] Thanks to the high specific capacity (~250–300 mAh g^{-1})[19–21] and the high charging cut-off voltage (>4.6 V), lithium rich layered oxides (LRLOs) can provide high specific energy densities.[6,15,22,23] The excess Li in LRLO, hosted in the transition metal layer, contributes to the high specific capacity.

The structure of LRLOs can be described as a solid solution of two components: one $LiMO_2$ (M=Ni, Mn, and Co) phase with a space group of *R-3 m* corresponding to the basic structure of layered cathode materials and one Li_2MnO_3 phase with monoclinic space group of *C/2 m*.[22,24] The structural similarity owing to lattice parameters of the two phases (0.47 nm for both the (003) planes in trigonal $LiMO_2$ and the (001) planes of monoclinic Li_2MnO_3 phases) enables their coexistence.[22] The actual distribution of the two domains throughout the bulk structure, however, is still unclear.[22,25–32] The activation of the Li_2MnO_3 component at high potentials (>4.4 V)[19] provides

[a] H. Choi, A. R. Schuer, H. Moon, G.-T. Kim, J. Asenbauer, A. Kazzazi, M. Kuenzel, S. Passerini
Helmholtz Institute Ulm (HIU) Electrochemical Energy Storage, Helmholtzstrasse 11, 89081 Ulm, Germany
E-mail: matthias.kuenzel@kit.edu
stefano.passerini@kit.edu

[b] H. Choi, A. R. Schuer, H. Moon, G. Melinte, G.-T. Kim, J. Asenbauer, A. Kazzazi, M. Kuenzel, S. Passerini
Karlsruhe Institute of Technology (KIT), P.O. Box 3640, 76021 Karlsruhe, Germany

[c] G. Melinte
Institute of Nanotechnology (INT) Hermann-von-Helmholtz-Platz 1, 76344, Eggenstein-Leopoldshafen, Germany

Supporting information for this article is available on the WWW under https://doi.org/10.1002/celc.202400391

additional capacity through oxygen anion oxidation reaction after the transition metal redox reaction.[26,33,34] In the voltage profile up to ~4.4–4.5 V, the cationic redox reaction of transition metals ($Ni^{2+/3+/4+}$ and $Co^{3+/4+}$) manifests as a slope. The additional capacity from the irreversible oxidation of oxygen can be seen as a long plateau in the first charging profile.[22] However, the contribution of oxygen redox O^{2-}/O^{2-x} comes at the expense of structural instability, which results in the irreversible capacity loss occurring in the 1st cycle.[35–37] Additionally, the oxygen redox reaction at high potentials facilitates the migration of Ni^{2+} ions into vacant Li sites, which aggravates upon cycling.[38,39] The relocated Ni^{2+} ions in the Li layer hinder the re-insertion of Li ions and trigger the layered phase deformation leading to spinel-like and finally rock-salt structure upon extended cycling. This is accompanied by severe capacity fading and voltage decay.[40]

Cobalt is known to offers enhanced structural stability, rate capability and cycling stability to NCM and other cathode materials.[9,41–43] Therefore, it is commonly used in LRLOs, such as $Li_{1.2}Ni_{0.133}Co_{0.133}Mn_{0.544}O_2$, to enhance the phase stability by reducing the effects of the oxygen redox process.[44,45] In this work, different amounts of Co in LRLOs are introduced ($Li_{1.2}Mn_{0.6-x/2}Ni_{0.2-x/2}Co_x$, x = 0, 0.04, and 0.08) by hydroxide co-precipitation and high temperature solid-state reaction. The physical and electrochemical properties of the synthesized LRLOs with different Co content were assessed and later correlated by *ex-situ* analysis. Finally, the performance of optimized Co-free LRLO is demonstrated superior to that of Co-containing materials.

Table 1. Chemical composition determined by ICP-OES of as-synthesized materials.

Sample	Target	Experimental
Co00	$Li_{1.20}Ni_{0.2}Mn_{0.6}O_2$	$Li_{1.20}Ni_{0.19}Mn_{0.61}O_2$
Co04	$Li_{1.20}Ni_{0.18}Mn_{0.58}Co_{0.04}O_2$	$Li_{1.20}Ni_{0.17}Mn_{0.59}Co_{0.04}O_2$
Co08	$Li_{1.20}Ni_{0.16}Mn_{0.56}Co_{0.08}O_2$	$Li_{1.21}Ni_{0.15}Mn_{0.57}Co_{0.07}O_2$

Results and Discussions

The chemical composition of as-synthesized LRLO active materials is determined by inductively coupled plasma - optical emission spectroscopy (ICP-OES) (Table 1). As listed, all the samples have compositions close to the target ones. Note that the samples are named after their Co content in the structure (i.e., Co00 for the Co-free sample, and Co04 and Co08 for the samples containing 4% and 8% of Co, respectively).

Scanning electron microscopy (SEM) images of the samples at different magnifications are shown in Figure 1. Secondary particles, consisting of agglomerates of primary particles, are seen in the low-magnification images (Figure 1a–c). These are irregular in shape and size, independent of the Co content. Also, no significant differences were found among LRLOs' primary particles regardless of Co contents (Figure 1d–e), in contrast with our previous work showing the strong influence of TM source on the morphology of LRLO.[46] In particular, the sulfate ($TM(II)SO_4 \cdot H_2O$) was found to produce smaller primary particles during co-precipitation when compared to acetate

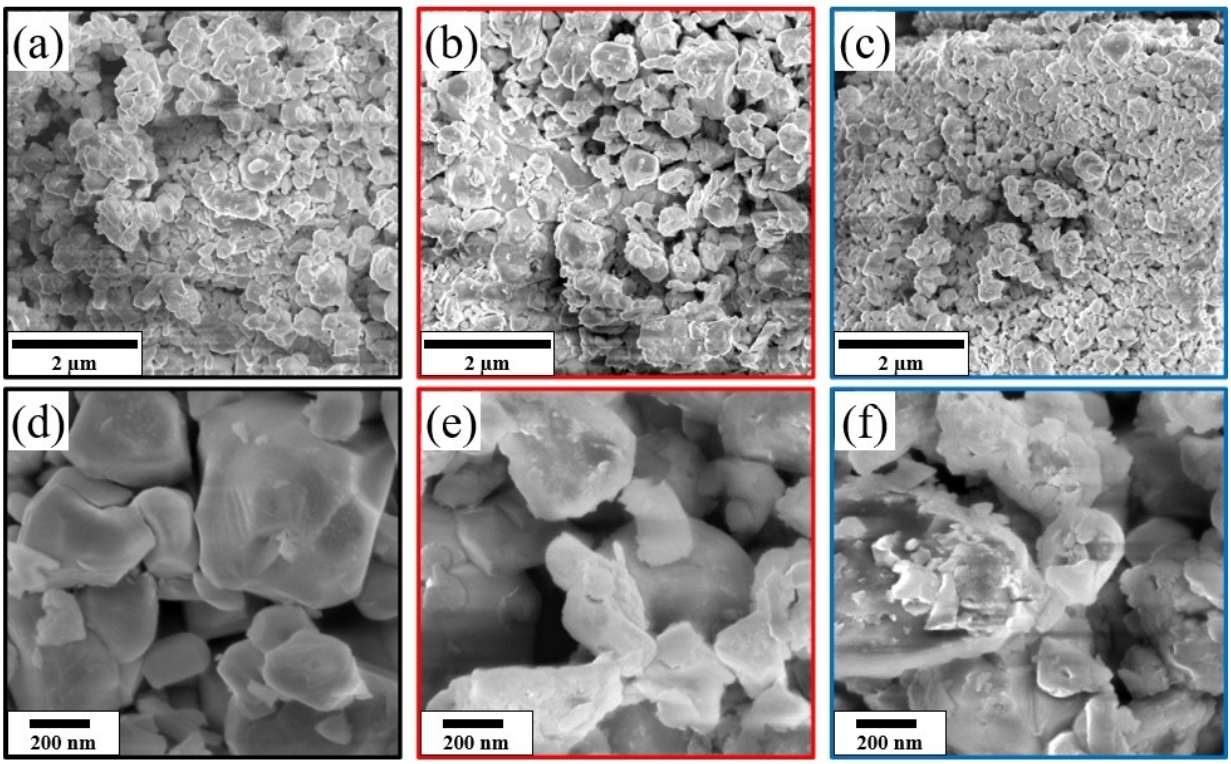

Figure 1. SEM micrograph of (a, d) Co00, (b, e) Co04, and (c, f) Co08 at different magnifications.

$(TM(II)(CH_3COO)_2 \cdot nH_2O)$ producing bigger particles. This suggests that the choice of TM source is highly influential to the morphology of LRLO, whereas the amount of Co during precursor formation has almost no impact on the morphology.

The influence of the Co content on the crystallographic structure of the LRLO samples is investigated by comparing powder XRD patterns (Figure 2a–c). The identical XRD patterns of all materials confirm that they all crystallized in the trigonal structure (and hexagonal layered α-$NaFeO_2$) with *R-3 m* space group, i.e., the basic layered structure ($LiMO_2$) without any impurity. The peaks (indicated by asterisks) between ~20–23° are ascribed to the (020), (110), and (111) reflections of the superstructure, originating from the ordering of Li and Mn ions in the TM layers of the Li_2MnO_3 component of the LRLO, which crystallizes in the *C/2 m* space group.[47,48] To obtain quantified structural parameters, Rietveld refinement was conducted (Table 2, other refined information of the samples are given in Table S1, Table S2, Table S3, and Table S4). In Figure 2d, the changes of the lattice parameter *a* and the unit cell volume are displayed. Furthermore, the ratio between the lattice parameter *c/3a* and the degree of cation mixing along the Co content are visualized in Figure 2e. The lattice parameter, *a* (*b* as $a = b$ in *R-3 m*) tends to increase with decreasing Co content because of the cationic substitution of Co^{3+} ($r(Co^{3+}) = 0.545$ Å) with Mn^{4+} and Ni^{2+} ($r(Mn^{4+}) = 0.53$ Å and $r(Ni^{2+}) = 0.69$ Å).[49] Crystallite size and unit cell volume of the materials reduced considerably with higher Co content as displayed in Table 2. The *c/3a* ratio, a commonly used parameter to estimate the fineness of the layered structure,[50,51] is found to increase with increasing Co content. At the same time, cation mixing is decreasing with

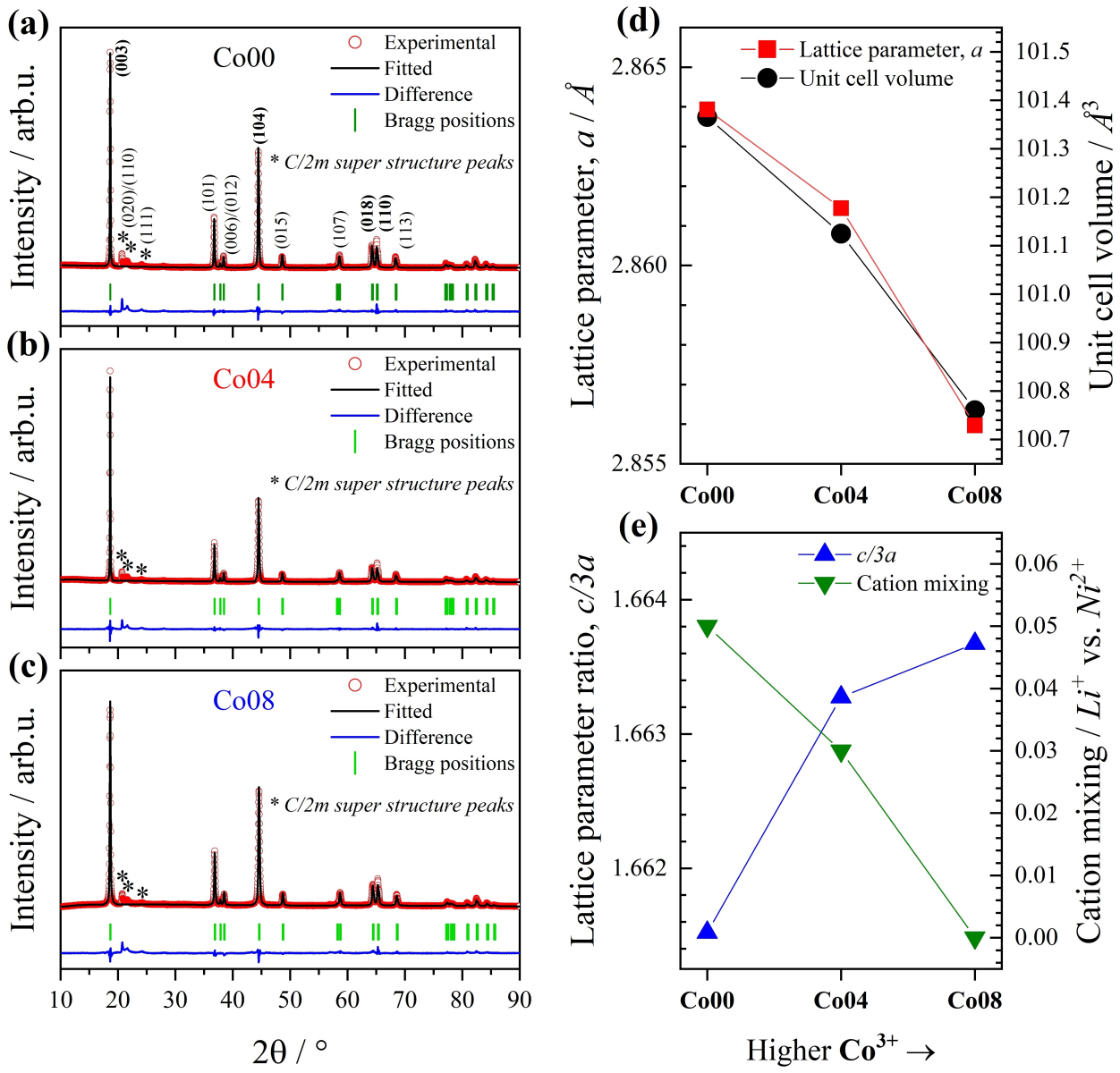

Figure 2. Powder XRD patterns of (a) Co00, (b) Co04, and (c) Co08 and Rietveld refinement parameters (d) *a* lattice parameter and unit cell volume and (e) lattice parameter ratio *c/3a* and cation mixing (Li^+ vs. Ni^{2+}) of Co00, Co04 and Co08.

Table 2. Refined structural parameters from the XRD patterns of Co00, Co04 and Co08.

	Co00	Co04	Co08
Crystal system	Trigonal	Trigonal	Trigonal
Space group	R-3 m	R-3 m	R-3 m
Lattice parameter: *a*, *b* (Å)	2.864	2.861	2.856
Lattice parameter: *c* (Å)	14.28	14.28	14.26
Unit volume (Å^3)	101.38	101.18	100.73
Crystallite size (Å)	6622	1683	755
Cation mixing (Ni^{2+} in Li^+ layer)	0.05	0.03	0
Phase density (g cm^{-3})	4.19	4.12	4.16

higher amounts of Co^{3+}. While no cation mixing is shown for Co08, 5% of Ni^{2+}/Li^+ exchange is observed for the Co-free Co00. Accordingly, the information obtained from the refinement confirms Co to stabilize the layered structure of LRLOs by reducing cation mixing and providing improved ordering of the layered structure.

Besides acting as a structural stabilizer, Co promotes oxygen redox activity ($Co^{3+/4+}$:t_{2g} to O^{2-}:2p)[45,52] therefore contributing to a higher specific capacity of LRLOs. The voltage profiles and corresponding differential capacity plots from the materials' 1st charge/discharge cycle are given in Figure 3. At a first glance, the three electrode materials show a similar activity in the sloping region associated with the oxidation of the TMs (< 4.4 V), but capacities increasing with the Co content are observed in the high voltage plateau region (> 4.4 V).[53–56] The transition from the sloping to the plateau (indicated by dash-dot lines in Figure 3a) is easily distinguished in the differential capacity profiles as the region between the two intense oxidation peaks (Figure 3b). Similar capacities are obtained for the materials in the sloping region (106, 105, and 107 mAh g^{-1} for Co00, Co04 and Co08, respectively), as expected since for one $Co^{3+/4+}$ replacing $^1/_2$ $Ni^{2+/3+/4+}$ and $^1/_2$ inactive Mn^{4+} (see ICP results in Table 1). However, the capacity measured along the plateau increased from 197 to 202 and 212 mAh g^{-1} on going from Co00, Co04, and Co08, respectively, because the oxygen redox activity increases with the amount of Co (see Figure 3b inset). Although higher Co contents contribute to higher 1st cycle dis-/charge capacity, the highest Coulombic efficiency (CE) is achieved by the Co-free sample (80.6, 79.6, and 77.8% in Co00, Co04, and Co08, respectively). This can be attributed to the irreversible oxygen redox due to the overlap of the O^{2-}:2p band with the $Co^{3+/4+}$:t_{2g} band, which greatly accelerates the oxygen loss.[39,45,52]

The testing protocol for assessing the rate performance of LRLOs involved galvanostatic charge/discharge at current densities ranging from 0.1 C to 10 C (1 C = 250 mA g^{-1}) in the 2.5–4.8 V voltage window. The materials showed rather similar capacities and CEs up to 2 C (Figure 4a), however, both the Co-containing samples slightly outperformed the Co-free one at 5 C and 10 C. This is also confirmed in Figure 4b showing the materials specific capacities normalized to their discharge capacity in the 1st cycle at C/20. This is perfectly in line with the structural investigation (Figure 2e), revealing that the *c*-lattice parameter of LRLOs increased with the Co content, thus facilitating Li^+ diffusion in the layered structure.[51] Nonetheless, the high-rate performance difference is rather small, with Co00 offering rate performance comparable to those of Co04 and Co08. This is further confirmed by the materials voltage profile evolution at different current densities. The 3rd cycle at each current density was selected and the (dis−)charge capacity is normalized to unity at each current density (Figure 4c–e, data without normalization is shown in Figure S2). Increasing overpotentials are observed with increasing current densities, but all the samples exhibit very similar trends regardless of the Co content. Hence, the rate performance of all LRLOs does not appears to strongly depend on the Co content.

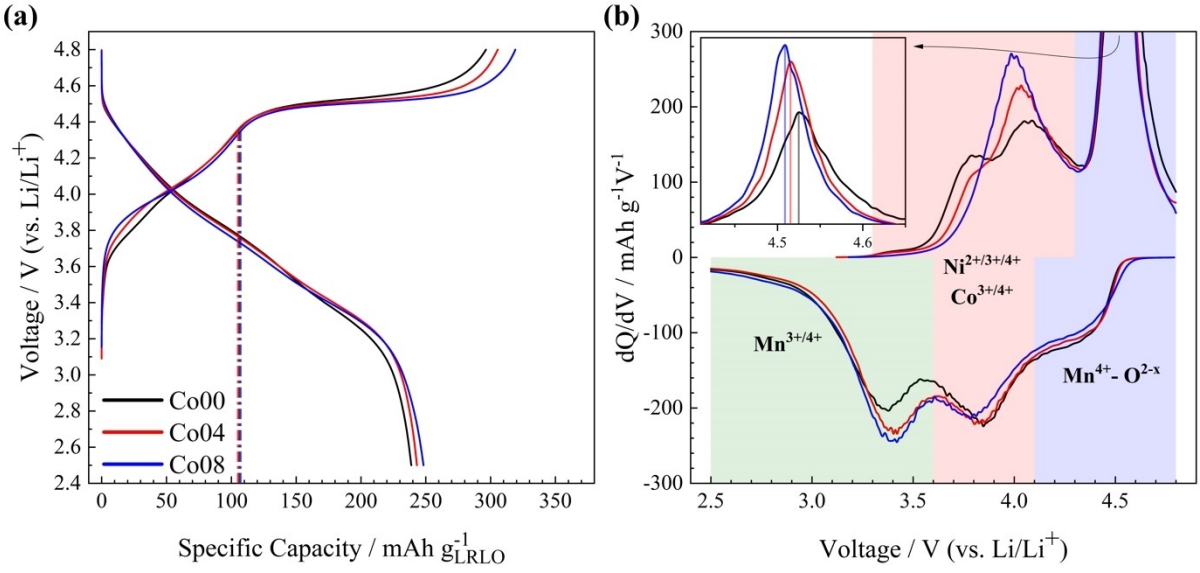

Figure 3. (a) Voltage profiles and (b) the differential capacity plots of Co00 (black), Co04 (red), and Co08 (blue) at the 1st cycle at C/20.

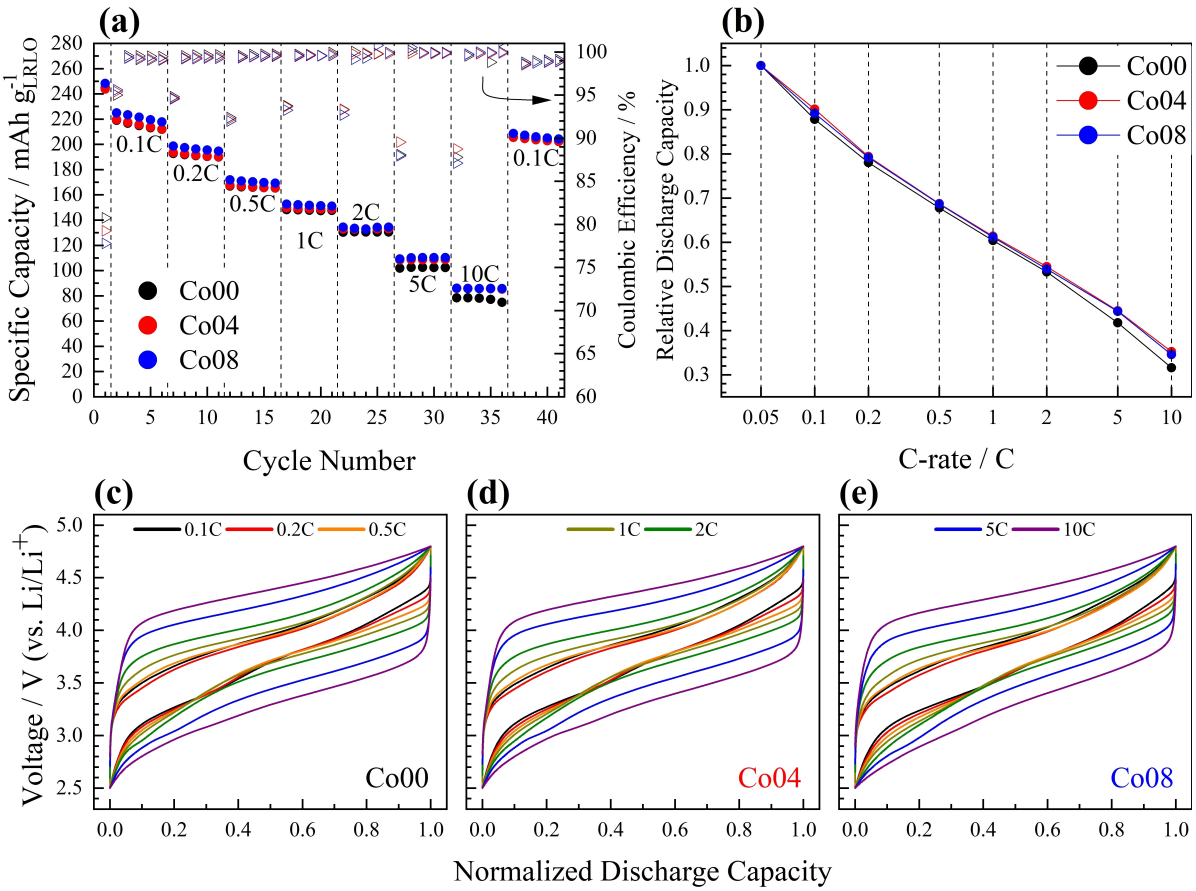

Figure 4. (a) Rate performance, (b) Relative discharge capacity at different C-rate normalized to the 1st cycle capacity at C/20 of Co00, Co04, and Co08. (c–e) Voltage profiles in the 3rd cycle at each current densities of Co00, Co04, and Co08. The capacity range is normalized to unity independent on the real capacity.

The long-term cycling stability of the materials was evaluated in terms of discharge specific capacity, CE, and dis-/charge working voltage over 300 cycles at 1 C (Figure 5). a few low-rate cycles at 0.1 C were applied every 100 cycles to compare the capacity evolution of the materials without kinetics effects. As observed in Figure 5a, Co08 delivered a higher initial discharge capacity (154.1 mAh g^{-1}) than Co00 (150.7 mAh g^{-1}). However, the Co-containing materials showed a lower stability upon the 300 cycles at 1 C, retaining only 84.3 % (Co04) and 75.9 % (Co08) whereas Co00 maintained 88.1 % of its initial capacity. Figure 5b compares the dis-/charge average voltage of the materials, which is the apparent bottle-neck of LRLOs for more extensive commercial applications. The gap (ΔV) between the average charge and discharge voltages (Figure 5 c–e) increased upon cycling for all materials, but the increase is faster and larger for the LRLOs containing Co. On the other hand, Co00 showed the lowest discharge voltage fading with only 235 mV (3.64 V→3.40 V) versus Co08 with 280 mV (3.60 V→3.32 V). Such a behavior is even more pronounced in the normalized capacity profiles in Figure S3. The same trends are observed at low rates, indicating that the voltage fading is not only due to kinetics.

Overall, Co00 exhibits a superior performance in terms of operation voltage as well as specific capacity. The differential specific capacity profiles in Figure S4 illustrate as all materials suffer from the oxidation peak shifting to higher potentials and the reduction peak shifting to lower potentials. Upon cycling, the Mn^{4+}–O^{2-x} redox peak slightly increased while the redox peak of $Ni^{2+/3+/4+}$ and $Co^{3+/4+}$ shifted to higher potentials upon charge regardless of the Co content. On the other hand, during discharge, the differential capacity profiles show a remarkable variation depending on whether LRLO contains Co or not. After the long-term cycling test, the TM redox peak is hardly distinguished in Co04 and Co08 whereas Co00 still retains the TM reduction peak at 3.43 V (3.84 V in the initial cycle). Furthermore, the $Mn^{3+/4+}$ redox process is more strongly activated in Co04 and Co08 than in Co00 (Figure 5b). However, the differential capacity plot of all materials at 0.1 C (Figure S4d–f) do not show large differences during charge as those observed at 1 C (Figure S4a–c). On the other hand, the TM ($Ni^{2+/3+/4+}$ and $Co^{3+/4+}$) reduction peaks lose intensity and their position shifts to lower potential during discharge. The activity of $Mn^{4+/3+}$ remains strong for Co04 and Co08 from the 2nd to 4th low-rate cycle steps, but the TM reduction peak faded already at 3rd low-rate cycle, leaving the $Mn^{3+/4+}$ redox as the primary redox couple.

X-ray photoelectron spectroscopy (XPS) analysis was carried out on Co00 and Co08 electrodes after 300 cycles at 1 C to analyze the composition of the formed cathode-electrolyte interphase (CEI) layer. The classification of chemical species in

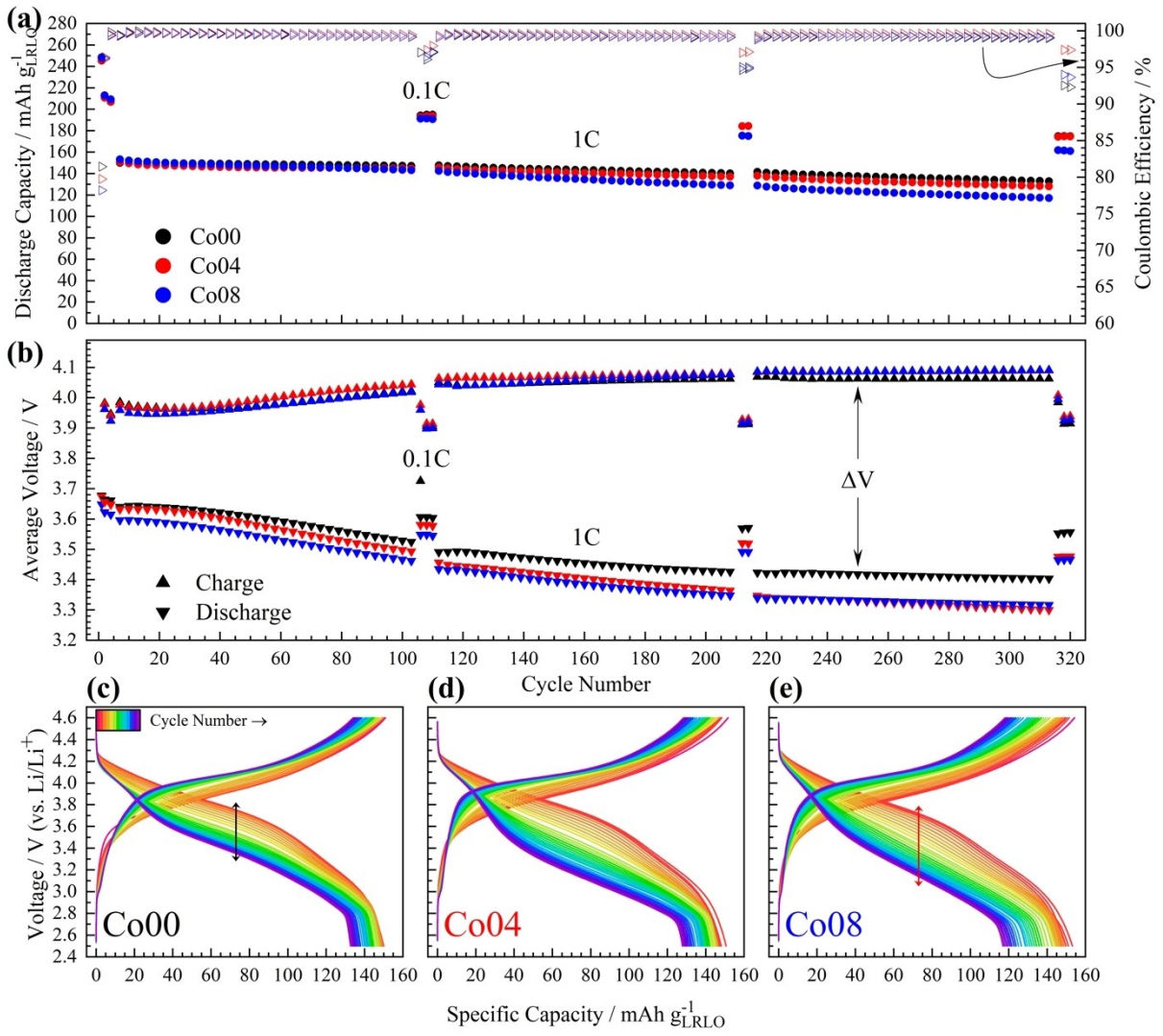

Figure 5. Galvanostatic cycling stability tests of Co00, Co04, and Co08 (1 C) followed by the activation cycle at C/20. Evolution of (a) specific discharge capacity, Coulombic efficiency and (b) dis-/charge voltage. Selected (every 10th cycle) voltage profiles of (c) Co00, (d) Co04, and (e) Co08.

the CEI follows our previous work with a few minor adjustments.[46] Figure 6a,b offer fittings of non-TM components (*i.e.*, the C 1s, O 1s and F 1s core level spectra of Co00 and Co08). For both the electrodes, similar carbon species (and relative contents) are found in the C 1s region. Namely, the peaks at 284.4 eV (C=C) and 285.0 eV (C–C/C–H) are the fingerprint of conductive carbon (Super C65). The peak at 286.7 eV can be assigned to C–O moieties from polyethylene oxide (PEO)-like species formed by EC polymerization and C*H_2–CF_2 bonds from the PVdF binder. Alkyl-carbonate-related species (O–C=O) appearing at 289.2 eV can be ascribed to by-products of the electrolyte. The last peak of the C 1s spectra around 290.1 eV can be assigned to both C*F_2–CH_2 from PVdF and to carbonate species $(CO_3)^{2-}$. The O 1s spectra share the oxygenated carbon species with the C 1s spectra: alkyl-carbonate-related species (O–C=O* at 532.1 eV and O*–C=O at 534 eV) and $(CO_3)^{2-}$ at 532.1 eV. The intensities of the oxygenated carbon species (except for C–O at 533.1 eV) are similar for both the materials. Likewise, the intensities of other oxygenated species, such as $Li_xPO_yF_z$ (~534.8 eV) and M–O (530 eV), are also comparable. This suggests that the chemical composition and thickness of the CEI on the two electrodes are highly alike. The higher C–O peak at Co08 may suggest a slightly higher degree of solvent decomposition, however, the difference is negligible. In the F 1s spectra, LiF and Li_xPF_y/CF_2 are assigned at 685.6 eV and 688.0 eV, respectively. To sum up the observation in C 1s, O 1s, and F 1s, no profound difference in the composition and concentration of the CEI species is found indicating that the two samples have almost identical CEI layer regardless of Co presence. Therefore, regardless of the Co content, the trend in the reaction between the LRLO electrode and the electrolyte are similar to each other.

Besides, the oxidation states of Mn in the samples' surface were investigated deconvoluting the Mn 2p core level spectra (Figure 6c).[57,58] The areal ratio of the Mn^{3+}/Mn^{4+} peaks is calculated as 1.50 and 1.65 for Co00 and Co08, respectively. The results indicate for a higher fraction of Mn^{3+} than Mn^{4+}, i.e., a lower oxidation state of Mn in Co08, suggesting that Co00

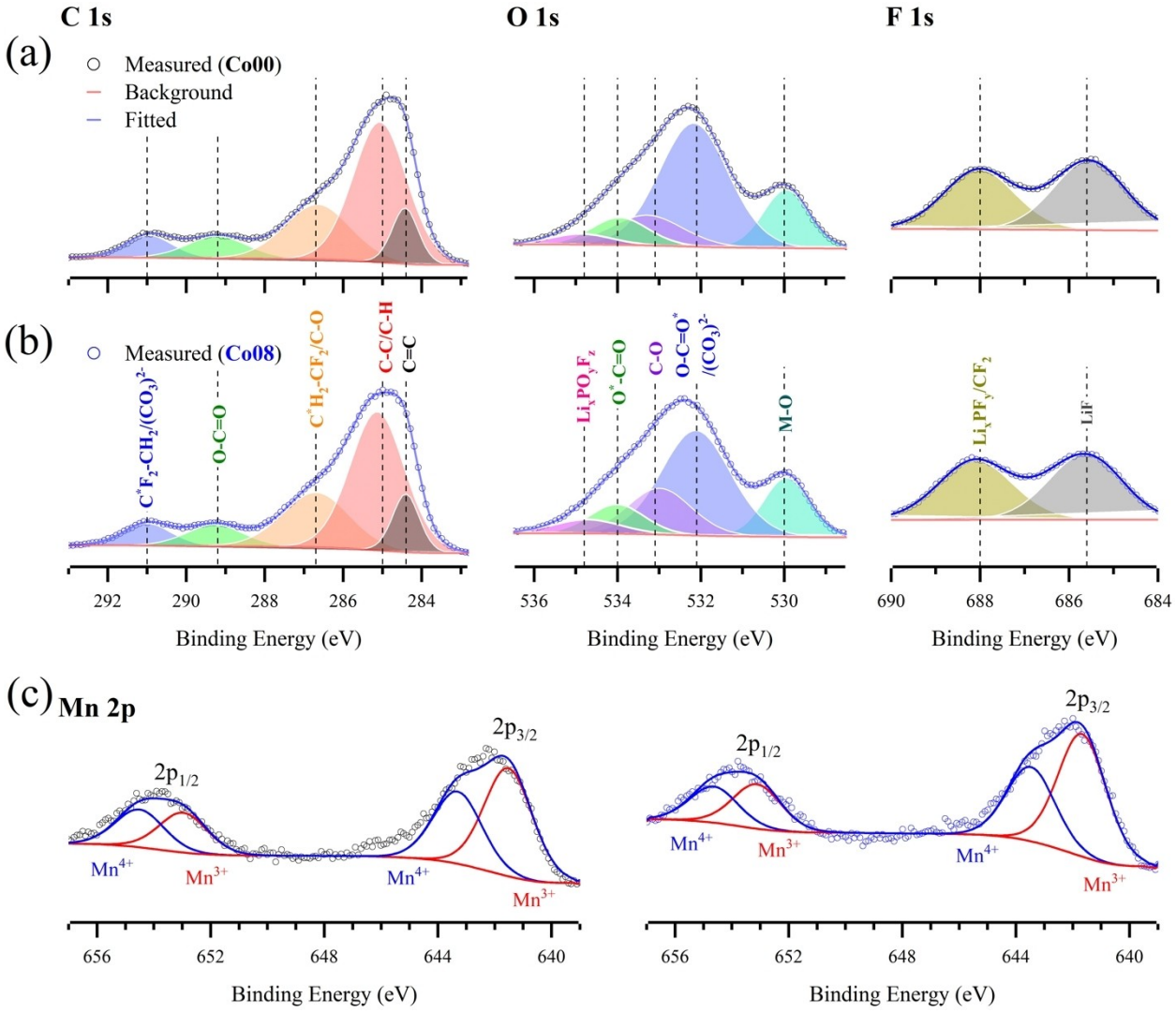

Figure 6. Photoelectron lines of C 1s, O 1s, and F 1s regions of (a) Co00 and (b) Co08 and (c) Mn 2p regions of Co00 (left) and Co08 (right) ex-situ electrodes. Electrodes were collected after 300 cycles at 1 C rate (discharged state). Measured data points are marked with black and blue hollow circles for Co00 and Co08, respectively.

retains more stable Mn^{4+} on the surface in the lithiated state after long-term cycling. This is in good agreement with the trend of differential specific capacity (Figure S4), where Co-containing Co08 and Co04 show a larger contribution of the $Mn^{4+/3+}$ redox upon long-term cycling.

The Co00 and Co08 *ex-situ* electrodes were also subjected to XRD characterization to investigate the structural changes occurring upon cycling (Figure 7). The diffraction patterns of the electrodes after 300 cycles maintain their original shape (except for the disappearance of the reflections in the range of ~20–25 2θ°), indicating that the fine layered structure does not change upon cycling (Figure 2). The magnified areas (see Figure 7c) show as the features of Co00 are located at higher 2θ angles compared to Co08, indicating for smaller lattice parameters of Co08 after cycling. Considering that pristine Co08 has the smallest values in *a*-, *b*-lattice and unit volume, *V* (Table 2), Co00 might experience the most intense structural densification over cycling. Also, Co08 shows higher and sharper peaks implying that its structural characteristics are well maintained after long-term cycling, which is further confirmed by the clear peak splitting of the (110) peak. On the other hand, the merged (110) peak for Co00 suggests for a variation of its structure after long-term cycling.

Electron energy loss spectroscopy (EELS) was conducted for the Co00 and Co08 powders as made (Figure 8a,b) and harvested from the cycled electrodes (Figure 8c,d). A series of spectra were obtained by line scanning from the outermost surface towards the bulk (as indicated within arrows in Figure S5) with a total depth of ~19 nm at a resolution of ~1 nm. The fine structure of the O–K edge reflects the properties of lattice oxygen and the cumulative oxidation environment of the TM.[59,60] In combination with TM EELS, it is possible to determine changes in the chemical state (*i.e.*, Mn oxidation state) by comparing the analysis of pristine (fresh) and post-mortem samples.[61] Regarding pristine Co00 and Co08, both materials show a distinguished pre-peak at the outermost

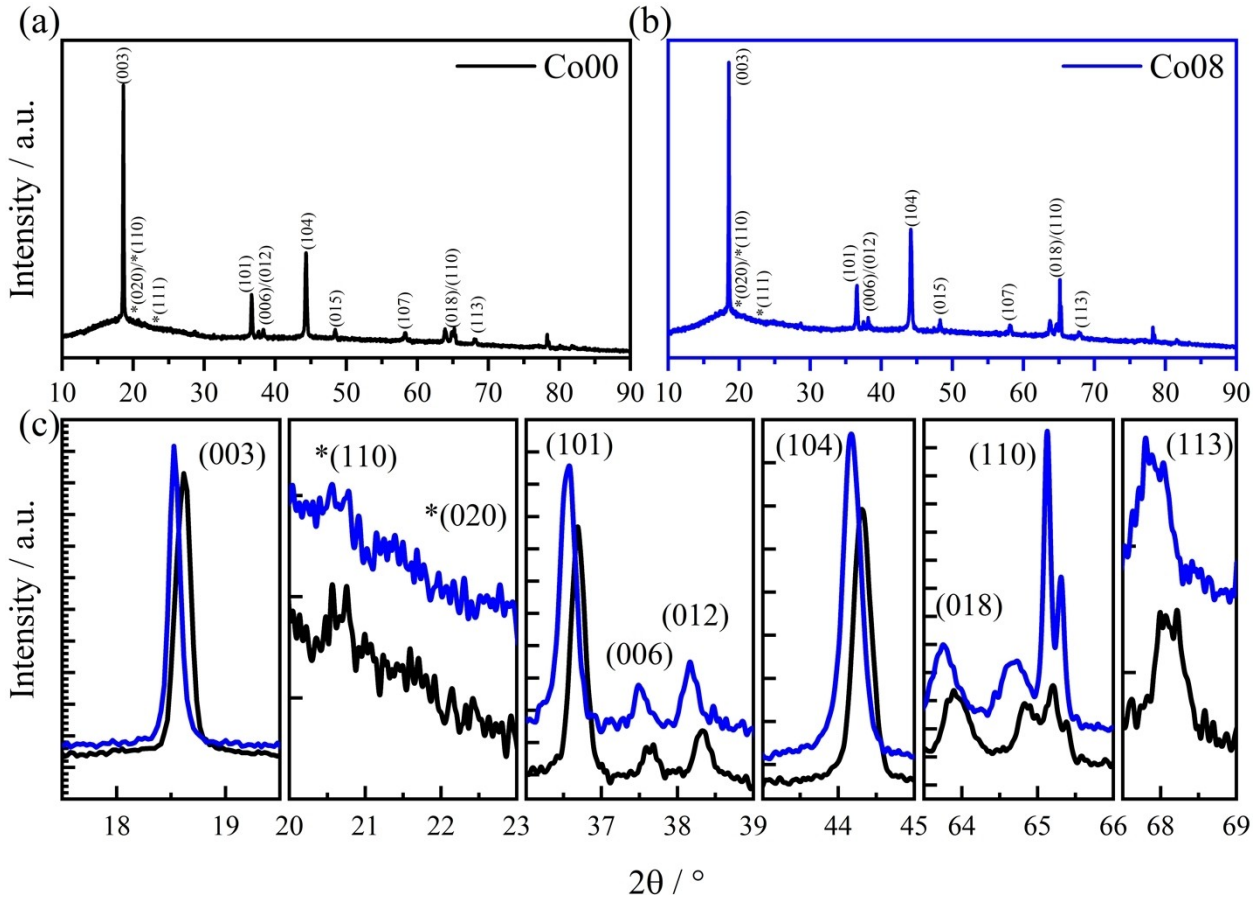

Figure 7. *Ex-situ* XRD patterns of the cycled electrodes in discharged state after 300 cycles at 1 C of (a) Co00 and (b) Co08, and (c) magnified peaks of Co00 (black) and Co08 (blue).

surface in the O–K edge spectra (marked by asterisks (*) in Figure 8a,b). After cycling (Figure 8c,d), the pre-peak cannot be found at the surface, but appears going further in the bulk at ~5–6 nm for Co00 (Figure 8c) and ~10 nm for Co08 (Figure 8d). Regarding the Mn–L_3 edge, the presence of a shoulder at lower energies suggests a mixed-phase of Mn^{3+} and Mn^{4+}, while the symmetric peak at lower electron energy loss features dominant Mn^{3+} state.[62] In the Mn–L_3 edges in Figure 8a,b (magnification shown in Figure S6a,b), a shoulder near the surface region (~2–3 nm) is found for both Co00 and Co08 indicating the presence of the mixed-phase in the pristine powders. After 300 cycles, however, the shoulder disappears at the outermost surface to reappear for Co00 around ~9–10 nm (light green), while no shoulder is detected for Co08 until ~14 nm from the surface (light blue) (see Figure 8c,d and Figure S6c,d). The comprehensive interpretation of the O–K and Mn–L_3 edge fine structure supports for the cycled Co08 to have a lower Mn oxidation state, owing to the absence of lattice oxygen, and a thicker chemically modified layer than cycled Co00. Additionally, the shift of the L_3 peak (and the L_3/L_2 peak ratio) in the Mn- and Ni–L spectra (Figure 8e,f) on going from the surface into the bulk of the material, are well explained by the alteration of the chemical state. Going from the outermost to the innermost region, the chemical shift detected for the Mn–L edge of Co08 is 1.44 eV for the pristine powder and 3.42 eV for the cycled electrode, i.e., always higher than in Co00 (1.26 eV and 1.7 eV, respectively). The magnitude of the Ni–L_3 shift is lower than the Mn–L_3 shift with both pristine Co00 and Co08 exhibiting 0.18 eV. However, the latter material shows a much higher shift after cycling (0.54 eV) while the shift of the former remains unaltered. The L_3/L_2 ratio also supply information on the oxidation state of TMs being inversely correlated with the oxidation state of Mn.[62,63] The L_3/L_2 ratio of the Co00 and Co08 Mn–L peaks is rather similar and constant along the particle's depth, revealing that Mn in both the LRLOs is at a high oxidation state (Mn^{4+} rather than Mn^{3+}) on and near the surface. The Mn L_3/L_2 ratio after cycling is, however, slightly higher for Co08 at the outermost surface indicating a lower Mn oxidation state with respect to Co00. Considering the depth variation, the Mn L_3/L_2 ratio reverts to the pristine material's value faster for Co00, i.e., within ~7 nm, than for Co08 (~13 nm). This implies a thicker surface-reconstruction layer on Co08, in which Mn^{3+} becomes the main component. This is in good agreement with the previous XPS analysis showing a higher fraction of Mn^{3+} in Co08 than Co00. Furthermore, it is also in accordance with the pre-peak disappearing in the O–K edge spectra at deeper levels indicating for a lower oxidation state of Mn in Co08, possibly coupled to a lower oxygen

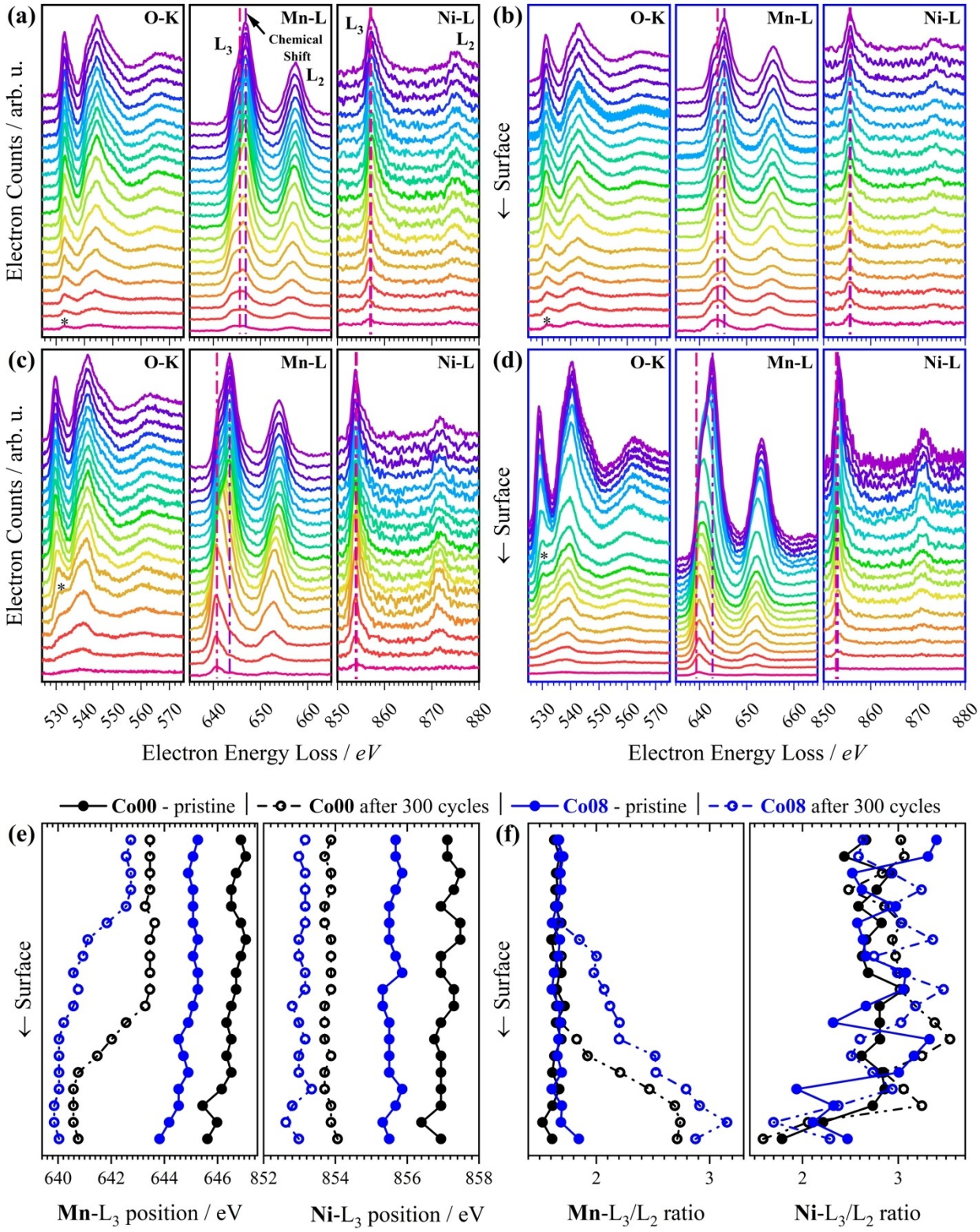

Figure 8. Series of EELS spectra of the O–K, Mn–L, and Ni–L edges of Co00 (a,c) and Co08 (b,d) powders as made (fresh) (a,b) and extracted from cycled electrodes (c,d). The electrodes' powders were collected after 300 cycles at 1 C (discharged state). Depth profile shifts of (e) the L_3 peak position and (f) the ratio of L_3/L_2 intensities at the Mn–L and Ni–L edges.

content on the surface. The Ni L_3/L_2 ratio shows a noisy behavior, with only a minor shift close to the surface for both materials, indicating that Ni in the high oxidation state exist only near the surface. In summary, EELS results indicate for a surface oxygen depletion occurring upon cycling, resulting in the presence of Mn^{3+}on the surface of LRLOs, especially in

Co08. This is expected to result in severe capacity fading and voltage decay, especially for Co08 as seen in Figure 5.

After the further optimization of LRLOs (Figure S1), full-cell tests of Co00 were carried out in three-electrode cells with graphite anode (N/P capacity ratio of 1.08). After the activation cycle at 0.1 C, the cells were subjected to 1000 galvanostatic cycles at 1 C without any constant voltage step. The initial discharge capacity of 180 mAh g^{-1} decreases to 153 and 134 mAh g^{-1} at the 500th and 1000th cycle, respectively (Figure 9a). The cell shows a capacity retention of 85% at the 500th cycle and 75% at the 1000th cycle. Importantly, the average discharge voltage is very stable with the average voltage at the 1000th cycle being 94% of the initial value (Figure 9b). The voltage evolution vs. specific capacity performance upon cycling is detailed in Figure 9c and in Figure 9d (in this latter the capacity is normalized to the maximum capacity at the cut-off voltage of 2.3 V). The voltage fading is mainly limited to lower potentials (< 3.4 V) because of a stronger involvement of the $Mn^{4+/3+}$ redox process. In general, this full-cell shows a highly stable cycling with moderate fading, presenting a very narrow distribution of normalized profiles in Figure 9d. The capacity fading of the cell is also moderate accounting to 85% and 75% at the 500th and 1000th cycle, respectively (Figure 9c). Finally, the energy density of the LRLO|Graphite full-cell, calculated with respect to the cathode and anode active materials' weight is given in Figure 9b. Thanks to the excellent retention both in specific capacity and average discharge

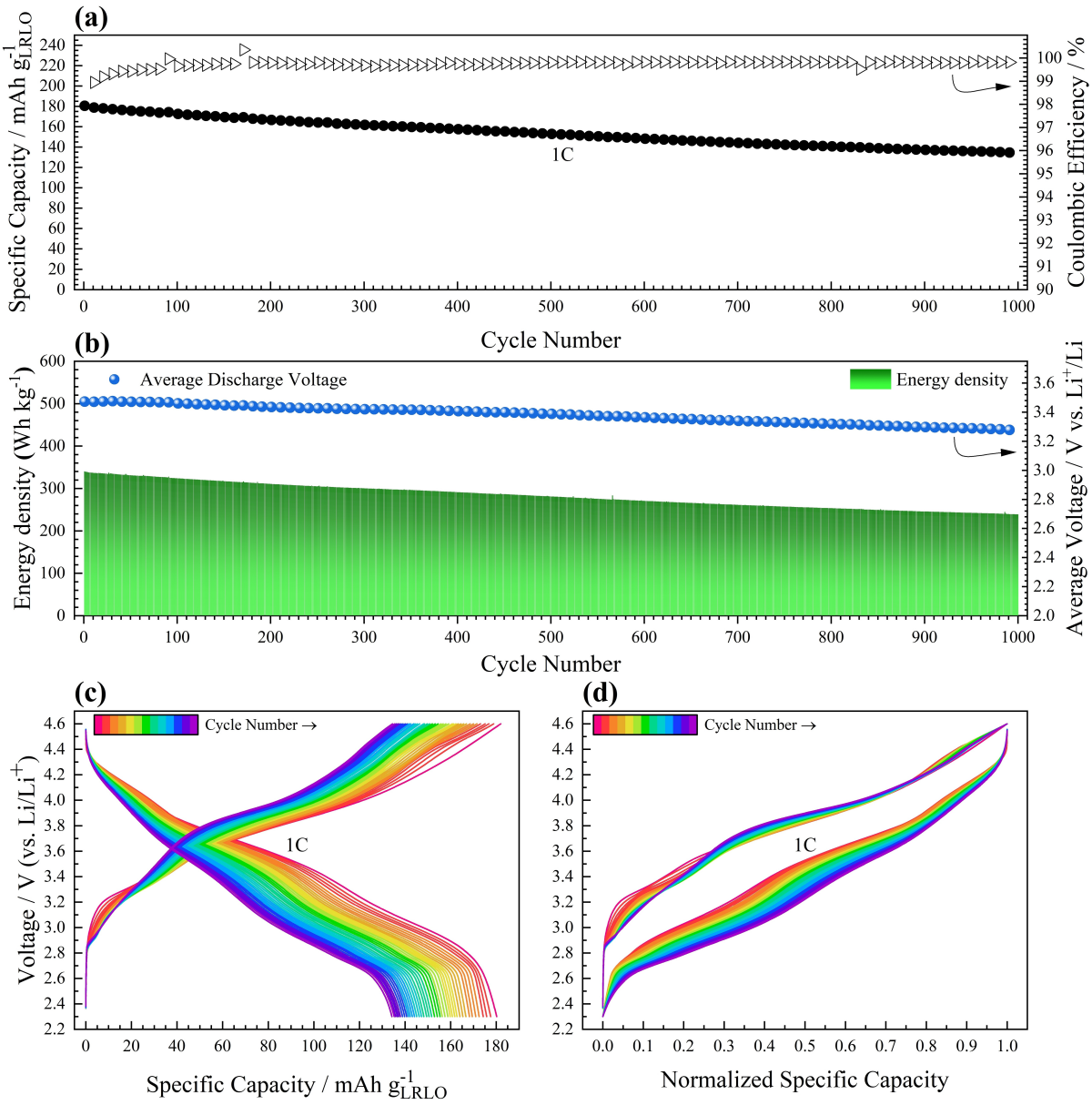

Figure 9. Galvanostatic cycling of a Co00 LRLO|LP30|Graphite full-cell at 1 C. Evolution of (a) specific discharge capacity and CE, (b) specific energy density and average discharge voltage. (c) Selected voltage profiles (every 10th cycle) and (d) selected voltage profiles (every 10th cycle) versus normalized specific capacity to each dis-/charge capacity.

voltage, 70.2% of the initial energy density is maintained even after 1000 cycles.

Conclusions

Herein, the effect of Co on the electrochemical performance of LRLO cathode active materials has been investigated. The Co content was adjusted to 0, 4, and 8% with respect to the overall TM. As the same synthesis procedure was applied for the three materials, no difference in morphological features was found. Rietveld refinement of the powder XRD patterns confirms the role of Co as a bulk structural stabilizer in LRLOs showing as the Co-containing materials exhibit higher crystallinity of the layered structure and lower cation mixing than the Co-free material. In electrochemical half-cell tests, Co08 (as the representative Co-containing material) delivers higher initial capacities than Co00 due to a more extended Mn^{4+}–O^{2-x} redox activation. However, the Co-containing LRLOs suffer from severe capacity and voltage fading upon extended cycling, while the Co-free material, Co00, demonstrated good rate performance and enhanced cycling stability in terms of both capacity and operating voltage.

The TM redox during discharge weakens upon cycling while the oxygen redox on charge and $Mn^{4+/3+}$ increases. However, this is determined to be more irreversible within Co-containing LRLOs while Co00 retains the activity of TM redox and moderate $Mn^{4+/3+}$ redox, contributing to a lower voltage fading. This was confirmed via *ex-situ* XPS analysis revealing that the main difference between the Co-free and Co-containing materials is the Mn oxidation state. Cycled Co08 shows a higher fraction of Mn^{3+} on the electrode surface and this is prevalent from the surface into the bulk as confirmed by EELS measurements. Interestingly, *ex-situ* XRD of cycled electrodes suggests that Co still stabilizes the layered bulk structure upon cycling as indicated by clearer XRD features. The Co-free composition shows excellent electrochemical performance in LRLO|graphite full-cell with an average discharge voltage retention of 94.3% and good specific capacity retention of 74.4% after 1000 cycles at 1 C. We conclude that Co stabilizes the layered structure in LRLOs, but it does not necessarily enhance the electrochemical performance. Rather, Co diminishes the electrochemical performance of LRLOs by promoting irreversible Mn^{4+}–O^{2-x} and $Mn^{4+/3+}$ redox on charge and discharge respectively, which accelerates the voltage fading well as accessible specific capacity.

Acknowledgements

The authors would like to acknowledge the financial support from the European Union within Si-Drive project. This project received funding from the European Union's Horizon 2020 research and innovation programme under grant agreement number 814464. The financial support of the Helmholtz Association is also acknowledged. Open Access funding enabled and organized by Projekt DEAL.

Conflict of Interests

The authors declare no competing financial interest.

Data Availability Statement

The data that support the findings of this study are available on request from the corresponding author. The data are not publicly available due to privacy or ethical restrictions.

[1] J.-M. Tarascon, M. Armand, *Nature* **2001**, *414*, 359–367.
[2] J. R. Croy, A. Abouimrane, Z. Zhang, *MRS Bull.* **2014**, *39*, 407–415.
[3] M. S. Whittingham, *Proc. IEEE* **2012**, *100*, 1518–1534.
[4] D. Deng, *Energy Sci. Eng.* **2015**, *3*, 385–418.
[5] H. Zhang, et al., . *J. Mater. Chem. A* **2018**, *6*, 20564–20620.
[6] N. Nitta, F. Wu, J. T. Lee, G. Yushin, *Mater. Today* **2015**, *18*, 252–264.
[7] Y. Zhang, et al., *Sci. China Technol. Sci.* **2015**, *58*, 1809–1828.
[8] C. Liu, Z. G. Neale, G. Cao, *Mater. Today* **2016**, *19*, 109–123.
[9] M. Li, J. Lu, *Science* **2020**, *367*, 979–980.
[10] A. Manthiram, J. C. Knight, S.-T. Myung, S.-M. Oh, Y.-K. Sun, *Adv. Energy Mater.* **2016**, *6*, 1501010.
[11] C. Banza Lubaba Nkulu, et al., *Nat. Sustain.* **2018**, *1*, 495–504.
[12] X. Fu, et al., *Environ. Sci. Technol.* **2020**, *54*, 2985–2993.
[13] J. Zheng, et al., *Adv. Energy Mater.* **2017**, *7*, 1601284.
[14] L. Nie, et al., *Nano Lett.* **2021**, *21*, 8370–8377.
[15] H. Zhao, et al., *Nano Energy* **2022**, *92*, 106760.
[16] Y. Fan, et al., *Angew. Chem.* **2023**, *135*, e202213806.
[17] H. Zhao, et al., *Adv. Energy Mater.* **2022**, *12*, 2103894.
[18] Y. Fan, et al., *ACS Energy Lett.* **2024**, *9*, 487–496.
[19] D. Kim, et al., *J. Electrochem. Soc.* **2013**, *160*, 0–7.
[20] C. S. Johnson, N. Li, C. Lefief, M. M. Thackeray, *Electrochem. Commun.* **2007**, *9*, 787–795.
[21] B. Qiu, et al., *Nat. Commun.* **2016**, *7*, 1–10.
[22] M. M. Thackeray, et al., *J. Mater. Chem.* **2007**, *17*, 3112.
[23] M. M. Thackeray, et al., *Sustain. Energy Fuels* **2018**, *2*, 1375–1397.
[24] Z. Lu, D. D. MacNeil, J. R. Dahn, *Electrochem. Solid-State Lett.* **2001**, *4*, A191–A194.
[25] J. Rana, et al., *J. Electrochem. Soc.* **2016**, *163*, A811–A820.
[26] K. A. Jarvis, Z. Deng, L. F. Allard, A. Manthiram, P. J. Ferreira, *Chem. Mater.* **2011**, *23*, 3614–3621.
[27] C. S. Johnson, et al., *Electrochem. Commun.* **2004**, *6*, 1085–1091.
[28] M. M. Thackeray, S. H. Kang, C. S. Johnson, J. T. Vaughey, S. A. Hackney, *Electrochem. Commun.* **2006**, *8*, 1531–1538.
[29] J. Bareño, et al., *Chem. Mater.* **2011**, *23*, 2039–2050.
[30] J. R. Croy, et al., *J. Power Sources* **2012**, *159*, A781–A790.
[31] J. Rana, et al., *J. Mater. Chem. A* **2014**, *2*, 9099–9110.
[32] R. E. Ruther, A. F. Callender, H. Zhou, S. K. Martha, J. Nanda, *J. Electrochem. Soc.* **2015**, *162*, A98–A102.
[33] K. A. Jarvis, Z. Deng, L. F. Allard, A. Manthiram, P. J. Ferreira, *J. Mater. Chem.* **2012**, *22*, 11550–11555.
[34] N. Yabuuchi, K. Yoshii, S. T. Myung, I. Nakai, S. Komaba, *J. Am. Chem. Soc.* **2011**, *133*, 4404–4419.
[35] A. R. Armstrong, et al., *J. Am. Chem. Soc.* **2006**, *128*, 8694–8698.
[36] N. Yabuuchi, K. Yoshii, S. Myung, I. Nakai, S. Komaba, *J. Am. Chem. Soc.* **2011**, 4404–4419.
[37] J. Hong, et al., *Chem. Mater.* **2012**, *24*, 2692–2697.
[38] J. Reed, G. Ceder, A. Van Der Ven, *Electrochem. Solid-State Lett.* **2001**, *4*, A78.
[39] X. Xiang, J. C. Knight, W. Li, A. Manthiram, *J. Phys. Chem. C* **2014**, *118*, 21826–21833.
[40] J. Li, et al., *J. Power Sources* **2011**, *196*, 4821–4825.
[41] Y. K. Sun, et al., *Nat. Mater.* **2009**, *8*, 320–324.
[42] H.-J. Noh, S. Youn, C. S. Yoon, Y.-K. Sun, *J. Power Sources* **2013**, *233*, 121–130.
[43] H.-H. Ryu, K.-J. Park, C. S. Yoon, Y.-K. Sun, *Chem. Mater.* **2018**, *30*, 1155–1163.
[44] T. Ohzuku, A. Ueda, *J. Electrochem. Soc.* **1994**, *141*, 2972–2977.
[45] A. Manthiram, A. Vadivel Murugan, A. Sarkar, T. Muraliganth, *Energy Environ. Sci.* **2008**, *1*, 621.

[46] H. Choi, A. R. Schuer, H. Moon, M. Kuenzel, S. Passerini, *Electrochim. Acta* **2022**, *430*, 141047.
[47] Z. Lu, Z. Chen, J. R. Dahn, *Chem. Mater.* **2003**, *15*, 3214–3220.
[48] J. Bréger, et al., *J. Solid State Chem.* **2005**, *178*, 2575–2585.
[49] C. C. Wang, A. Manthiram, *J. Mater. Chem. A* **2013**, *1*, 10209–10217.
[50] C. Yu, G. Li, X. Guan, J. Zheng, L. Li, *Electrochim. Acta* **2012**, *61*, 216–224.
[51] C. Yu, H. Wang, X. Guan, J. Zheng, L. Li, *J. Alloys Compd.* **2013**, *546*, 239–245.
[52] T. Ohzuku, *J. Electrochem. Soc.* **2006**, *141*, 2972.
[53] P. Rozier, J. M. Tarascon, *J. Electrochem. Soc.* **2015**, *162*, A2490–A2499.
[54] M. Sathiya, et al., *Nat. Mater.* **2013**, *12*, 827–835.
[55] S. Bhowmick, et al., *Science* **2015**, *350*, 1516–1522.
[56] M. Saubanère, E. McCalla, J. M. Tarascon, M. L. Doublet, *Energy Environ. Sci.* **2016**, *9*, 984–991.
[57] H. Li, et al., *Ionics* **2020**, *26*, 3785–3794.
[58] M. Kowalik, R. Zalecki, A. Kołodziejczyk, *Acta Phys. Pol. A* **2010**, *117*, 277–280.
[59] L. Yu, M. Li, J. Wen, K. Amine, J. Lu, *Mater. Chem. Front.* **2021**, *5*, 5186–5193.
[60] H. Tan, J. Verbeeck, A. Abakumov, G. Van Tendeloo, *Ultramicroscopy* **2012**, *116*, 24–33.
[61] M. Varela, et al., *Phys. Rev. B: Condens. Matter Mater. Phys.* **2009**, *79*, 1–14.
[62] H. Kurata, C. Colliex, *Phys. Rev. B* **1993**, *48*, 2102–2108.
[63] T. Riedl, T. Gemming, K. Wetzig, *Ultramicroscopy* **2006**, *106*, 284–291.

Manuscript received: May 31, 2024
Revised manuscript received: June 23, 2024
Version of record online: ■■, ■■

RESEARCH ARTICLE

In this manuscript it is shown as the presence of cobalt in Li-rich, layered oxide (LRLO) cathode materials is the main cause of the voltage and capacity fading, thus resulting detrimental for the long-term performance of lithium cells including it.

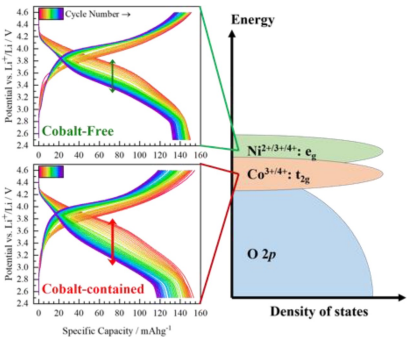

H. Choi, A. R. Schuer, H. Moon, G. Melinte, G.-T. Kim, J. Asenbauer, A. Kazzazi, M. Kuenzel, S. Passerini**

1 – 13

Is Cobalt in Li-Rich Layered Oxides for Li-Ion Batteries Necessary?